DOI: https://doi.org/10.24425/amm.2025.154485

A. DJORDJEVIĆ⁰^{1*}, M. ČOLOVIĆ⁰¹, M. ZEČEVIĆ⁰¹, D. TOŠKOVIĆ⁰², D. MINIĆ⁰¹

EFFECT OF CHEMICAL COMPOSITION ON THE CORROSION RESISTANCE, MICROSTRUCTURE, HARDNESS AND ELECTRICAL CONDUCTIVITY PROFILES OF THE Ag-Ge-SN ALLOYS

This study presents the results of experimental and analytical tests on the corrosion resistance of binary (Ge50Sn50, Ag50Sn50, Ag50Ge50) and ternary (Ag-Ge-Sn) alloys in 3% NaCl and microstructure, hardness, and electrical properties of the selected ternary Ag-Ge-Sn alloys. Alloys were prepared and analyzed using scanning electron microscopy and energy dispersive spectrometry (SEM-EDS), X-ray powder diffraction (XRD), Brinell hardness testing, and electrical conductivity measurements. Corrosion resistance was evaluated using potentiodynamic polarization (Tafel plots) and electrochemical impedance spectroscopy (EIS), with data fitted using DC Corrosion Technique and Gamry Echem Analyst software. The mechanical properties of the samples is strongly influenced by their phase composition. The study also includes the calculation of the equilibrium phase diagram of the Ag-Ge-Sn system on 25 and 500°C using the Calphad method and the Pandat program. By comparing predicted isothermal sections and experimental results a good agreement has been reached. Hardness and electrical conductivity values were measured and predicted across the full composition range using an appropriate mathematical model.

Keywords: Metals and alloys; electrical properties; mechanical properties; scanning electron microscopy (SEM); thermodynamics

1. Introduction

The study of ternary systems based on Ge-Sn attracts a lot of attention. Increased attention to the research of these alloys can be attributed to the specific properties of the Ge and Sn elements, such as good insulating properties, easy machinability, forging and many others. Understanding the phase diagrams of ternary systems involving Ge and Sn, along with their corrosion, mechanical, and electrical properties, is crucial due to their wide range of applications in energy, electronics, and other practical fields [1-3]. Moreover, alloys based on Ge are essential for advancing memory materials [4], as well as for manufacturing optical discs, DVDs, Blu-ray discs, flash memory, and more [5-9]. Our group has previously conducted studies on the ternary Ag-Ge-Sn system [10]. In our previous study reliable thermodynamic description has been proposed and experimentally confirmed with experimental investigation alloys from three vertical sections (Ag-GeSn, Ge-AgSn and Sn-AgGe) and two isothermal sections at 200 and 300°C. The experimentally determined results were used for the thermodynamic modeling of the ternary system. New ternary parameters for the liquid phase were introduced, and good agreement was achieved between the calculated phase diagrams and the experimental results. Additionally, our research group has investigated this ternary system from the aspect of its chemical and physical properties [11,12]. Since reliable thermodynamic description has been obtained by previous studys [10-12], in the current study same thermodynamic parameters has been used for calculations of the two isothermal sections at 25 and 500°C. Thermodynamic calculations of the isothermal sections were performed by using Pandat software [13]. Calculated phase diagrams of the isothermal sections were compared with experimental results done in current study. The following experimental techniques were used for experimental trials of this ternary system: scanning electron microscopy (SEM) and energy dispersive spectrometry (EDS), X-ray powder diffraction (XRD), hardness measurements by Brinell method and electrical conductivity measurements. In addition to the experimental test, the thermodynamic calculation of equilibrium diagrams of the state of ternary system was performed using the CALPHAD method. For each phase present in the examined system, the thermodynamic model and the values of thermodynamic parameters that occur in it were determined.

Corresponding author: coadjordjevic90@gmail.com



UNIVERSITY OF PRISHTINA IN KOSOVSKA MITROVICA, FACULTY OF TECHNICAL SCIENCE, KNJAZA MILOŠA 7, SERBIA

 $^{^2 \}quad \text{UNIVERSITY OF EAST SARAJEVO, FACULTY OF TECHNOLOGY, ZVORNIK, BOSNIA AND HERZEGOVINA} \\$

2. Experimental procedure

For the preparation of the binary and ternary alloys under investigation, high-purity Ag, Ge, and Sn supplied by Alfa Aesar (Germany) were used. The elements were precisely weighed in various molar ratios. The total mass of the samples was 7 g for corrosion resistance tests and 3 g for other analyses. These samples were melted and remelted five times in an induction furnace, under a high-purity argon atmosphere. The average mass loss during the melting process was approximately 1%. Following melting, the samples were divided into three groups. The first group was used for SEM-EDS analysis, hardness testing, and electrical conductivity measurements. The second group was subjected to corrosion resistance testing. The third group was annealed at 500°C for six weeks and was then analyzed using XRD and SEM-EDS. SEM-EDS analysis was performed with a JEOL JSM-6460 scanning electron microscope equipped with energy dispersive spectroscopy (EDS) from Oxford Instruments (X-act). Powder XRD data were recorded using a D2 PHASER (Bruker, Karlsruhe, Germany). Hardness was measured with a Brinell hardness tester (INNOVATEST, model NEXUS 3001), and electrical conductivity was assessed using the Foerster SIG-MATEST 2.069 eddy current instrument.

Scheme of experimental procedure has been presented on Fig. 1.

Samples from group 1 and 3 are prepared by classical experimental procedure as it is described in our previous papers [14,15].

While samples for corrosion test were prepared as follow. Three binary $Ge_{50}Sn_{50}$, $Ag_{50}Sn_{50}$, $Ag_{50}Ge_{50}$ and six ternary $Ag_{45}Ge_{10}Sn_{45}$, $Ag_{30}Ge_{40}Sn_{30}$, $Ag_{65}Ge_{17.5}Sn_{17.5}$, $Ag_{80}Ge_{10}Sn_{10}$, $Ag_{25}Ge_{25}Sn_{50}$, $Ag_{15}Ge_{15}Sn_{70}$ alloys were selected for measurement of corrosion resistance. The weight of the tested alloys was 7 g and the dimension were 15 mm \times 15 mm \times 1 mm. The corrosion resistance of these materials was examined in 3% NaCl solution using the potentiodynamic polarization method and electrochemical impedance spectroscopy (EIS). Tafel polarizing plots were fitted using the DC Corrosion Technique software. The results of electrochemical impedance spectroscopy (EIS) were fitted using the Gamry Echem Analyst program and the appropriate equivalent circuit.

Electrochemical tests of the corrosion resistance of the alloys in 3% NaCl solution were conducted using potentiodynamic polarization measurements (Tafel diagrams) and measurements of electrochemical impedance spectroscopy (Nyquist diagrams), on a potentiostat/gavanostat /ZRA Gamry Series G^{TM} 750 with an appropriate software.

Measurements were performed in a classic three-electrode electrochemical cell with a saturated calomel electrode (SCE) as a reference electrode, a Winkler platinum mesh as an auxiliary-

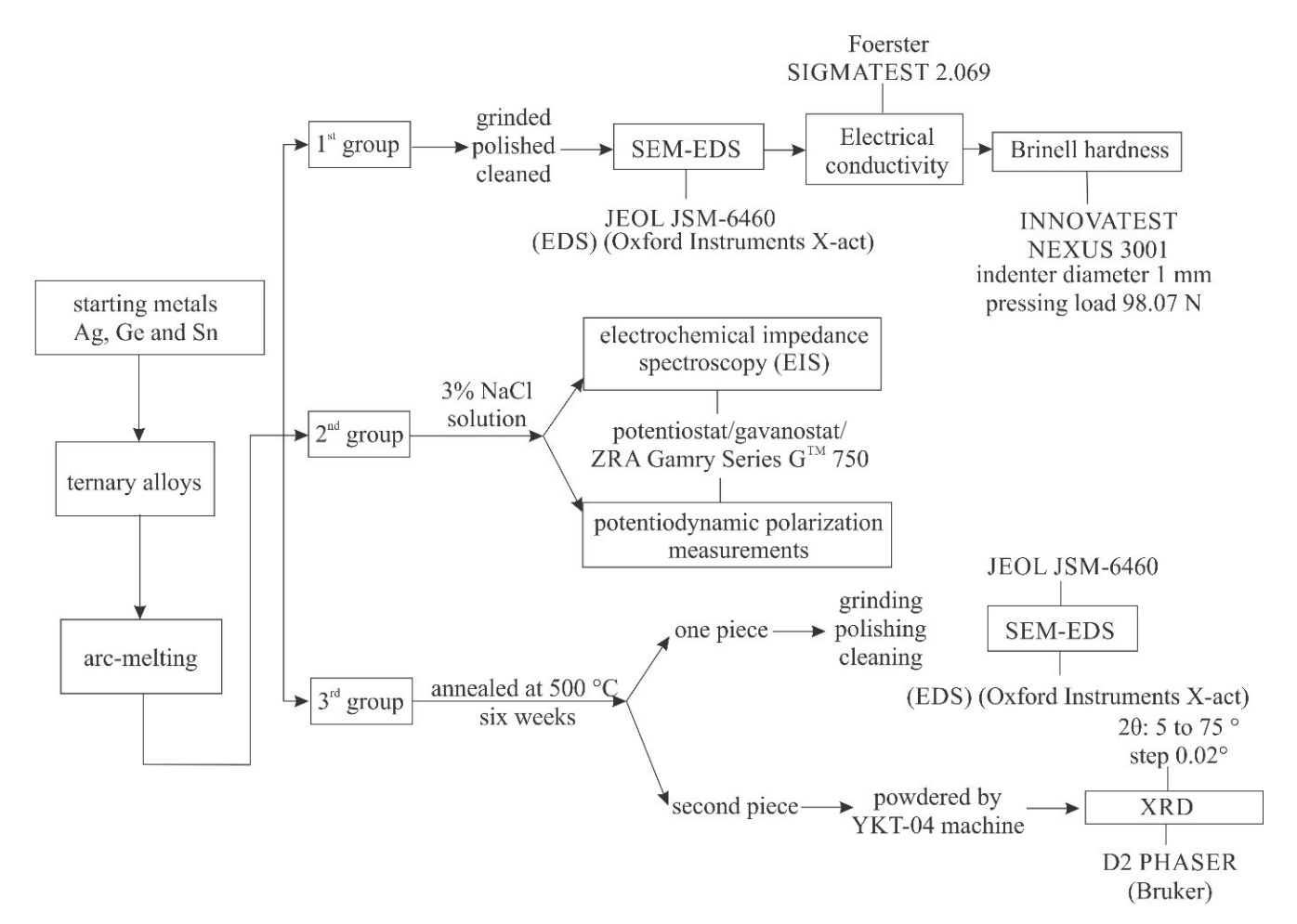


Fig. 1. Scheme of experimental procedure

counter electrode, and electrodes from the tested binary and ternary alloys as working electrodes.

The working electrodes are rectangular with a working surface of 1 cm². Immediately before the electrochemical test, the surfaces of the working electrodes were ground and polished. The samples were grinded on the Knut-Rotor-Struers device. Polishing was done on a DP-U3-Struers polishing device with diamond paste and finally cleaned in an ultrasonic bath and then wiped with alcohol.

Before starting the measurement, the potential of the open circuit E (OCP) was determined. After immersion in the electrolyte solution (3% NaCl), the working electrode was left at the open circuit potential for 1800 s until the stable corrosion potential, $E_{_corr}$ was established. After reading the corrosion potential, the working electrode is polarized. The electrode was first polarized in the cathode direction from $E_{_corr}$ to -250 mV, and then in the anodic direction from $E_{_corr}$ to 250 mV, where the rate of change of potential was (scan rate) 1 mV/s. The tests were performed at a constant temperature of 25°C (\pm 0.3°C) by controlling the cell temperature with a water bath.

Tafel plots were fitted using a DC Corrosion Technique software. The Tafel plots obtained by anodic and cathodic polarization in a wide range of potentials from the corrosion potential ($E = E_{_corr} \pm 250$ mV) are shown graphically in the semi-logarithmic form of the $\log j$ (A cm⁻²) $f E/V_{vs}$. SCE (Dependence of current density on potential (vs. SCE – saturated Calomel electrode). By extrapolating the anode and cathode Tafel lines in their cross section, the corrosion potential of $E_{_corr}$ and the corrosion current of $I_{_corr}$ are determined, which is used to calculate the corrosion rate – corrosion resistance [16].

After the establishment of a stable corrosion potential, the measurement of the electrochemical impedance was done by imposing on the working electrode a sinusoidal potential of amplitude (scan rate) of 10 mV/s in the frequency range 0.01-100000 Hz with ten points per decade.

The experimental results were fitted in the Gamry Echem Analyst program using an appropriate equivalent circuit.

Based on the values of electrochemical impedance at very high and very low frequencies, the value R_{po} was obtained, which further serves to calculate the corrosion current density, i.e. the corrosion rate of the metal [17,18].

By fitting the experimental results, electrochemical corrosion parameters are obtained: R_{sol} – electrolyte resistance,

 R_{po} –pore resistance (formed on the electrode / electrolyte surface), R_{cor} – polarization resistance or charge transfer resistance, C_c – double layer capacity – film capacitance, C_{cor} – electrochemical capacitance.

Electrochemical methods for corrosion resistance testing are described in detail in the relevant literature [19-21].

At least three polarization and impedance measurements were performed for each tested sample, with good repeatability. This paper presents representative results of performed electrochemical measurements.

3. Results and discussions

According to the previous study [10] and information about binary systems [22-27] in the ternary Ag-Ge-Sn system six solid phases, one liquid and one gas phase should appear. One is liquid phase and six are solid phases. List of solid phases with their crystallographic data is given in TABLE 1.

3.1. Microstructural analysis of samples from the first group

Twelve ternary samples were selected to SEM-EDS test. Overall compositions of samples were situated along three vertical sections (samples 1 to 4, along Ag-GeSn vertical section, samples 5-8 along Ge-AgSn vertical section and samples from 9-12 along Sn-AgGe vertical section). Results of EDS test were summarized in TABLE 2.

The nominal composition and the actual alloy composition determined by EDS are found to be in close agreement. EDS analysis was used to determine the composition of the phases present in the microstructures. The compositions of these phases are summarized and listed by phase name in TABLE 2.

The results indicate that the same three phases were detected in all ten samples. These phases are identified as (Ge), (β Sn), and ε . As reported in our previous study [11], SEM microstructures for samples 1 and 5 are shown for reference in Figs. 2a) and 2b). In the microstructure of sample 3, three phases were identified. EDS analysis revealed that these phases are (Ge), ε , and ζ . The microstructure of sample 3 is shown in Fig. 2c). Sample 4 contains two phases in its microstructure, which were

TABLE 1 Considered phase, their crystallographic data and database names for the solid phases of the ternary Ag-Ge-Sn system [22-27]

Thermodynamic	Phase	Pearson	Space	Lat	Lattice parameters (Å)			
database name	Filase	symbol	group	а	b	c	Ref.	
LIQUID	L	_				_		
FCC_A1	(Ag)	cF4	$Fm\overline{3}m$	4.08626			[22]	
BCT_A5	(βSn)	tI4	I4 ₁ /amd	5.8318		3.1819	[23]	
DIAMOND_A4	(aSn)	cF8	$Fd\overline{3}m$	6.4892			[24]	
DIAMOND_A4	(Ge)	cF8	$Fd\overline{3}m$	5.65675			[25]	
HCP_A3	ζ	hP2	P6 ₃ /mmc	2.9658		4.7842	[26]	
AG3SN	ε-Ag ₃ Sn	oP8	Pmmn	5.968	4.7802	5.1843	[27]	

No.	co	oy nomi mpositi mic frac	on		npositio es by EI %)		Determined phases by SEM-EDS
	x(Ag)	x(Ge)	x(Sn)	x(Ag)	x(Ge)	x(Sn)	SEM-EDS
1	0.2	0.4	0.4	20.2	39.7	40.1	(Ge) (βSn) ε
2	0.4	0.3	0.3	39.8	30.2	30.0	(Ge) (βSn) ε
3	0.65	0.175	0.175	65.0	17.6	17.4	(Ge) ε ζ
4	0.8	0.1	0.1	79.2	10.3	10.5	(Ge) ζ
5	0.45	0.1	0.45	45.2	9.5	45.3	(Ge) (βSn) ε
6	0.3	0.4	0.3	29.8	39.2	31.0	(Ge) (βSn) ε
7	0.2	0.6	0.2	20.5	60.2	19.3	(Ge) (βSn) ε
8	0.1	0.8	0.1	10.1	80.9	9.0	(Ge) (βSn) ε
9	0.4	0.4	0.2	40.8	40.7	18.5	(Ge) (βSn) ε
10	0.3	0.3	0.4	29.2	30.2	40.6	(Ge) (βSn) ε
11	0.25	0.25	0.5	24.4	25.2	50.4	(Ge) (βSn) ε
12	0.15	0.15	0.7	15.6	14.2	70.2	(Ge) (βSn) ε

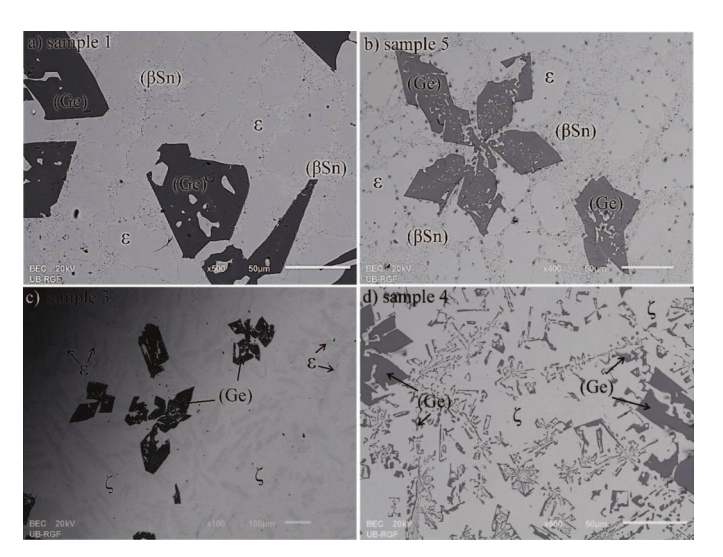


Fig. 2. SEM BSE micrographs of the a) sample 1, b) sample 5, c) sample 3 and d) sample 4 [11]

identified as (Ge) and ζ . The microstructure of sample 4 is shown in Fig. 2d).

SEM microstructures of samples 1, 5, 3 and 4 are presented as an illustration in Fig. 2 [11].

In all presented microstructures occurs solid solution (Ge) phase. In microstructures 1 and 5, beside (Ge) solid solution occurs ε phase and (β Sn) phase. Sample 3 contains three phases (Ge), ζ and ε . In microstructure of sample 4, two phases are visible, germanium and ζ phase.

By using compiled thermodynamic data set from reference [10], it is calculated isothermal section at 25°C. Composition of samples 1 to 12 are marked on calculated isothermal section and illustrated on Fig. 3.

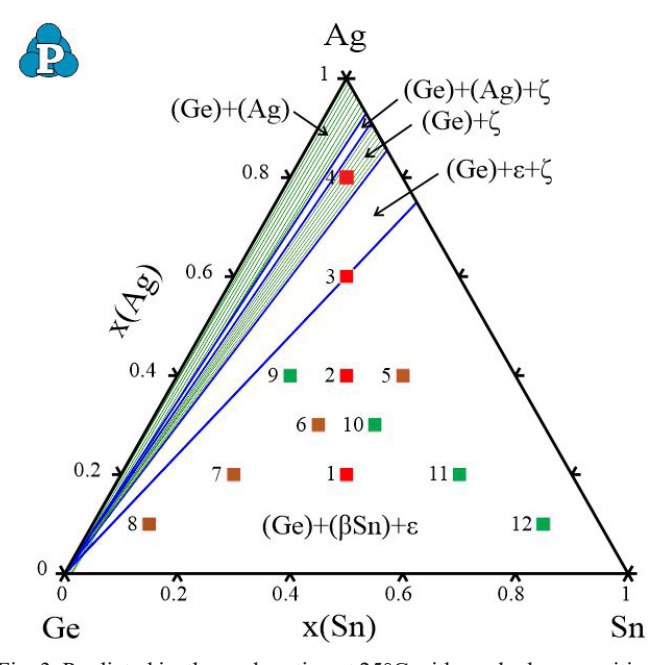


Fig. 3. Predicted isothermal section at $25^{\circ}\mathrm{C}$ with marked compositions of tested alloys

Five different phase regions are presented on calculated isothermal section at 25°C. Two are two-phase regions ((Ge) + ζ and (Ge) + (Ag)) and three are three-phase regions ((Ge) + (β Sn) + ϵ , (Ge) + ϵ + ζ and (Ge) + (Ag) + ζ). By locating EDS composition of samples 1 to 12 on calculated isothermal section at 25°C it is confirmed that samples 1, 2, 5 to 12 belong to the (Ge) + (β Sn) + ϵ three-phase region, sample 3 to the (Ge) + ϵ + ζ three-phase region and sample 4 to the (Ge) + ζ two-phase region.

3.2. Brinell hardness measurements

Twelve ternary samples were subjected to the Brinell hardness test [11]. Brinell hardness measurements were performed at room temperature. The measurement results are summarized in TABLE 3 together with predicted volume fraction of the phases. Prediction of phases are calculated by Pandat software.

Relation between mean value of Brinell hardness and alloy composition are presented grafically on Fig. 4 [11].

TABLE 3
Compositions of the investigated samples at room temperature and related Brinell hardness values

N.	Volume fraction of the phase at 25°C (%)		sured v (MN/m²		Mean value (MN/m²)	
	phase at 25 C (70)	1	2	3	(14114/1117)	
B1	$50(Ge) + 50(\beta Sn)$				20.73 [26]	
1	$33(\beta Sn) + 40(Ge) + 27\varepsilon$	30.3	31.5	31.8	31.2	
2	$17(\beta Sn) + 30(Ge) + 53\varepsilon$	71.9	73.0	72.8	72.5	
3	$17(Ge) + 53\varepsilon + 30\zeta$	112.9	120	116	116.3	
4	$10(Ge) + 90\zeta$	165.5	180.6	161.8	169.3	
Ag	100(Ag)				24.5 [27]	
B2	$33(\beta Sn) + 67\varepsilon$	28.2	33.1	34.6	31.9	
5	$30(\beta Sn) + 10(Ge) + 60\varepsilon$	38	40.1	38.1	38.7	
6	$20(\beta Sn) + 40(Ge) + 40\varepsilon$	64.6	72.3	66.8	67.9	
7	$13(\beta Sn) + 60(Ge) + 27\varepsilon$	150.2	145.7	149.8	148.5	
8	$7(\beta Sn) + 80(Ge) + 13\varepsilon$	196.4	203.7	202.8	201	
Ge	100(Ge)				973.40 [27]	
В3	50(Ag) + 50(Ge)				92.6 [28]	
9	$7(\beta Sn) + 40(Ge) + 53\varepsilon$	76.2	79.8	79.5	78.5	
10	$30(\beta Sn) + 30(Ge) + 40\varepsilon$	55.8	52.9	55.1	54.6	
11	$42(\beta Sn) + 25(Ge) + 33\varepsilon$	37.9	38	39.2	38.3	
12	$65(\beta Sn) + 15(Ge) + 20\varepsilon$	21.9 22 20.8		21.5		
Sn	100(βSn)				51 [27]	

In sample 8, Ag₁₀Ge₈₀Sn₁₀, the measured hardness is 201 MN/m². The high hardness of sample 8 is attributed to its microstructure, which consists of three phases: 80% (Ge), 7% (β Sn), and 13% ε . In the microstructures of samples 1, 2, and 5-12, the same three phases are present as in sample 8, though these samples show a trend of decreasing hardness compared to sample 8. This trend can be linked to the presence of the (βSn) and ε phases. In sample 3, the dominant phase is ε (53%), and its measured hardness is 116.3 MN/m². Sample 4 has a twophase structure, with (Ge) and ζ phases identified. The ζ phase is dominant in sample 4, making up 90% of the microstructure. The hardness of sample 4 is 169.3 MN/m², which is higher than that of the other ternary alloys (except sample 8). This can be explained by the dominance of the ζ phase in its microstructure. Additionally, the presence of the ζ phase in sample 3 contributes to its lower hardness value of 116.3 MN/m². Overall, it can be concluded that the percentage of the (Ge) phase significantly influences the hardness values. Sample 8 exhibits the highest hardness compared to the other ternary samples, and the ζ phase is also a key contributor to the high hardness in sample 4. The hardness of the samples is strongly influenced by their phase composition. A higher proportion of the (Ge) phase leads to increased hardness. Conversely, the presence of (βSn) and ε phases is associated with lower hardness. Additionally, the ζ phase plays a significant role in hardness value. These findings indicate that (Ge) and ζ phases enhance hardness, while the (β Sn) and ε phases tend to reduce it.

Based on the obtained results, shown in TABLE 3 and appropriate mathematical model it can be predicted bihavior of Brinell hardness allong all composition range. Prediction of hard-

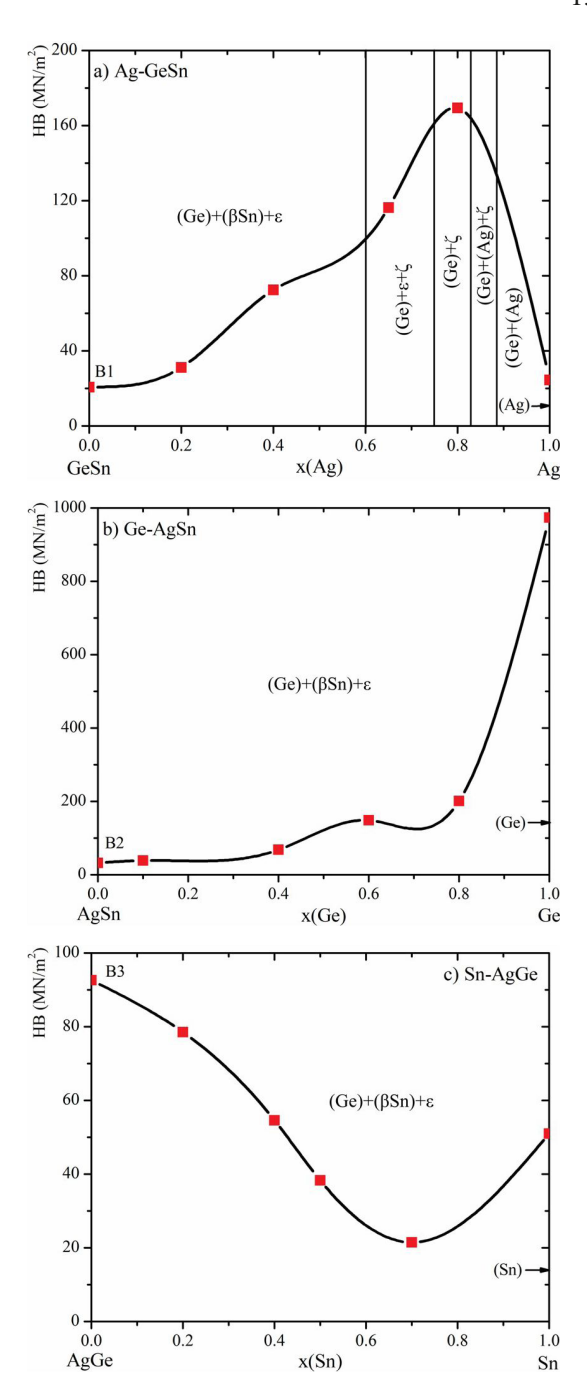


Fig. 4. Graphical presentation of Brinell hardness depending on the composition: a) vertical section Ag-GeSn, b) vertical section Ge-AgSn and c) vertical section *n*-AgGe [11]

ness is based on using Response Surface Methodology – RSM and software package Design Expert v.9.0.6.2.

Response Surface Methodology – RSM was used to quantify the relationship between independent input parameters and the dependent variable (response) [31-36].

For a three-component system, regression models can generally be formulated as polynomials defined by the following canonical or *Scheffé* forms:

Linear

$$\hat{y} = \sum_{i=1}^{q} \beta_i x_i \tag{1}$$

Quadratic

$$\hat{y} = \sum_{i=1}^{q} \beta_i x_i + \sum_{i < j}^{q-1} \sum_{i}^{q} \beta_{ij} x_i x_j$$
 (2)

Special Qubic

$$\hat{y} = \sum_{i=1}^{q} \beta_i x_i + \sum_{i < j}^{q-1} \sum_{j}^{q} \beta_{ij} x_i x_j + \sum_{i < j}^{q-2} \sum_{j < k}^{q-1} \sum_{k}^{q} \beta_{ijk} x_i x_j x_k$$
(3)

Full Cubic

$$\hat{y} = \sum_{i=1}^{q} \beta_i x_i + \sum_{i< j}^{q-1} \sum_{j=1}^{q} \beta_{ij} x_i x_j$$

$$+ \sum_{i< j}^{q-1} \sum_{j=1}^{q} \delta_{ij} x_i x_j (x_i - x_j) + \sum_{i< j}^{q-2} \sum_{j< k}^{q-1} \sum_{k}^{q} \beta_{ijk} x_i x_j x_k$$
(4)

· Special Quartic

$$\hat{y} = \sum_{i=1}^{q} \beta_{i} x_{i} + \sum_{i < j}^{q-1} \sum_{j}^{q} \beta_{ij} x_{i} x_{j} + \sum_{i < j}^{q-2} \sum_{j < k}^{q-1} \sum_{k}^{q} \beta_{iijk} x_{i}^{2} x_{j} x_{k}$$

$$+ \sum_{i < j}^{q-2} \sum_{i < k}^{q-1} \sum_{k}^{q} \beta_{ijjk} x_{i} x_{j}^{2} x_{k} + \sum_{i < j}^{q-2} \sum_{i < k}^{q-1} \sum_{k}^{q} \beta_{ijkk} x_{i} x_{j} x_{k}^{2}$$
(5)

· Full Quatric

$$\hat{y} = \sum_{i=1}^{q} \beta_{i} x_{i} + \sum_{i< j}^{q-1} \sum_{j}^{q} \beta_{ij} x_{i} x_{j} + \sum_{i< j}^{q-1} \sum_{j}^{q} \delta_{ij} x_{i} x_{j} (x_{i} - x_{j})$$

$$+ \sum_{i< j}^{q-1} \sum_{j}^{q} \gamma_{ij} x_{i} x_{j} (x_{i} - x_{j})^{2} + \sum_{i< j}^{q-2} \sum_{j< k}^{q-1} \sum_{k}^{q} \beta_{iijk} x_{i}^{2} x_{j} x_{k}$$

$$+ \sum_{i< j}^{q-2} \sum_{j< k}^{q-1} \sum_{k}^{q} \beta_{ijjk} x_{i} x_{j}^{2} x_{k} + \sum_{i< j}^{q-2} \sum_{j< k}^{q-1} \sum_{k}^{q} \beta_{ijjk} x_{i} x_{j} x_{k}^{2}$$

$$+ \sum_{i< j}^{q-3} \sum_{i< k}^{q-2} \sum_{k< l}^{q-1} \sum_{l}^{q} \beta_{ijkl} x_{i} x_{j} x_{k} x_{l}$$

$$(6)$$

Data processing was done in the software package Design Expert v.9.0.6.2. By utilizing experimentally determined values of hardness given in TABLE 3 mathematical model of the dependence of the Brinell hardness on composition for the Ag-Ge-Sn alloys was developed. Quadratic Mixture model has been suggested.

For the selected model, an analysis of variance (ANOVA-Analysis of Variance) is conducted [31-36].

ANOVA-Analysis of Variance confirmed the adequacy of the mathematical model. However, the diagnosis of the statistical properties of the assumed model found that the distribution of residuals is not normal and that it is necessary to transform the mathematical model in order to meet the conditions of normality. The Box-Cox diagnostics recommends the "Power" transformation for the variance stabilization.

The final equation of the predictive model in terms of real components is (7):

$$Ln (HB) = 3.94623547 \cdot (Ag) + 6.70578429 \cdot (Ge) + 3.7583475 \cdot (Sn) - 7.8742816 \cdot (Ge) \cdot (Sn)$$
 (7)

The obtained mathematical model is a *quadratic model* (Eq. 2) with computed values for the coefficients β_i and β_{ij} , where the components X_i and X_j are the mole fractions of the alloy components (Ag, Sn, and Ge). Coefficients that were not significant were eliminated from the model. The notation in parentheses, e.g., (Ag), represents the mole (or percentage) fractions of the individual components, and · denotes multiplication

The repeated analysis for Power model transformation confirms the significance of the Transformed Quadratic Mixture model. In this case, ANOVA confirms the adequacy of the Reduced Quadratic Mixture model (TABLE 4).

TABLE 4 ANOVA for Transformed Quadratic Mixture model

Source	Sum of Squares	df	Mean Square	F Value	<i>p</i> -value	
Model	12.43573	3	4.14524	17.08945	5.91579E-05	
Linear model	8.53387	2	4.26693	17.59114	0.00015	
BC	3.90186	1	3.90186	16.08608	0.00129	
Residual	3.39586	14	0.24256			
Cor Total	15.83159	17				

Terms in the ANOVA table:

- **Sum of Squares**: Sum of the squared differences between the average values for the blocks and the overall mean,
- **DF**: Degrees of freedom attributed to the blocks,
- Mean Square: Estimate of the block variance, calculated by the block sum of squares divided by block degrees of freedom.
- F Value: Test for comparing model variance with residual (error) variance.
- p-value (Prob > F): Probability of seeing the observed F value if the null hypothesis is true (there is no factor effect). Small probability values call for rejection of the null hypothesis.

The *F*-value of the Model is 17.09 and it implies that the model is significant. In this case, all model terms are significant. *R*-squared and other statistics after the ANOVA have appropriate values which confirm the justification of the adopted mathematical model (TABLE 5).

 $\label{eq:TABLE 5} TABLE \ 5$ R-squared and other statistics after the ANOVA

Std. Dev.	0.4925	R-Squared	0.7855
Mean	4.2172	Adj R-Squared	0.7395
C.V. %	11.6786	Pred R-Squared	0.6093
PRESS	6.1860	Adeq Precision	14.8266

Summary statistics for the model in the table 5 [35,36]:

- Std Dev: Square root of the residual mean square (an estimate of the standard deviation associated with the experiment).
- Mean: Overall average of all the response data.

- C.V.: Coefficient of Variation, the standard deviation expressed as a percentage of the mean. Calculated by dividing the Std Dev by the Mean and multiplying by 100.
- **PRESS**: Predicted Residual Error Sum of Squares A measure of how the model fits each point in the design.
- **R-squared**: A measure of the amount of variation around the mean explained by the model.
- Adj R-squared: A measure of the amount of variation around the mean explained by the model, adjusted for the number of terms in the model.
- **Pred** *R***-squared**: A measure of the amount of variation in new data explained by the model.
- Adequate Precision: This is a signal-to-noise ratio. It compares the range of the predicted values at the design points to the average prediction error.

The diagnosis of the statistical properties of the assumed model found that the distribution of residuals are normal. After the applied Box-Cox procedure [36], the value of λ is 0.0 k = 10. Therefore proving the justification of the model transformation.

Iso-lines contour plot for Brinell hardness of alloys defined by Eq. (7) is shown in Fig. 5.

3.3. Electrical conductivity measurements

Electrical conductivity was measured in the same samples as Brinell test [11]. TABLE 6 presents the results of measured values of electrical conductivity and their mean values.

The obtained results of electrical conductivity are also presented graphically. Fig. 6 shows a graphical representation of the relationship between electrical conductivity of the tested alloys and the composition of the alloys [11].

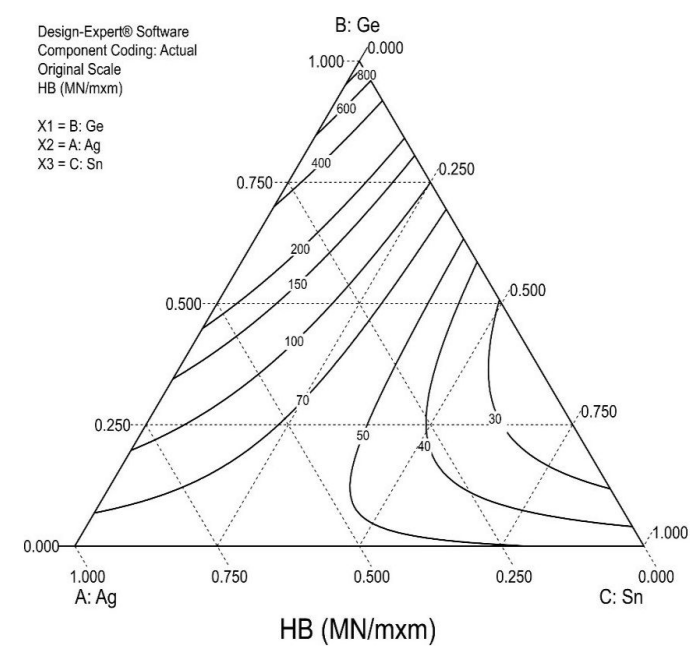


Fig. 5. Calculated iso-lines of Brinell hardness in ternary Ag-Ge-Sn system

Based on the results presented in TABLE 6 and Fig. 6a), it can be observed that the electrical conductivity values are generally low and fairly consistent across the samples. However, the conductivity values for samples 5 to 12 are higher than those for samples 1 to 4. The microstructures of samples 5 to 12 contain the same three phases: (β Sn), (Ge), and ε . Variations in the phase fractions contribute to slight differences in electrical conductivity. It can be concluded that the high percentage of ε is primarily responsible for the elevated electrical conductivity in the ternary alloys. Additionally, the (β Sn) phase also plays a role in contributing to the high conductivity values. Generally,

TABLE 6
Compositions of the investigated samples at room temperature and related electrical conductivity values

N.	Volume fraction of the phase		Measured v	alue (MN/m²)		Mean value (MN/m²)
N.	at 25°C (%)	1	2	3	4	Mean value (MIN/m)
B1	$50(Ge) + 50(\beta Sn)$					2.771 [26]
1	$33(\beta Sn) + 40(Ge) + 27\varepsilon$	1.342	1.350	1.344	1.348	1.346
2	$17(\beta Sn) + 30(Ge) + 53\varepsilon$	1.229	1.270	1.267	1.290	1.264
3	$17(Ge) + 53\varepsilon + 30\zeta$	1.745	1.768	1.637	1.910	1.765
4	$10(Ge) + 90\zeta$	1.998	2.010	1.973	1.989	1.998
Ag	100(Ag)					62.00 [35]
B2	$33(\beta \mathrm{Sn}) + 67\varepsilon$	9.196	9.190	9.186	9.143	9.179
5	$30(\beta Sn) + 10(Ge) + 60\varepsilon$	7.754	7.593	7.738	7.632	7.679
6	$20(\beta Sn) + 40(Ge) + 40\varepsilon$	4.651	4.877	4.531	4.560	4.655
7	$13(\beta Sn) + 60(Ge) + 27\varepsilon$	4.186	4.311	4.191	4.172	4.215
8	$7(\beta \mathrm{Sn}) + 80(\mathrm{Ge}) + 13\varepsilon$	3.110	2.978	2.874	2.994	2.989
Ge	100(Ge)					0.002 [35]
В3	50(Ag) + 50(Ge)					10.264 [28]
9	$7(\beta \mathrm{Sn}) + 40(\mathrm{Ge}) + 53\varepsilon$	7.687	7.800	7.736	7.742	7.741
10	$30(\beta \mathrm{Sn}) + 30(\mathrm{Ge}) + 40\varepsilon$	5.818	5.831	5.861	5.796	5.827
11	$42(\beta \text{Sn}) + 25(\text{Ge}) + 33\varepsilon$	5.746	5.541	5.626	5.434	5.587
12	$65(\beta Sn) + 15(Ge) + 20\varepsilon$	7.281	7.873	7.523	7.617	7.574
Sn	100(βSn)					9.1 [35]

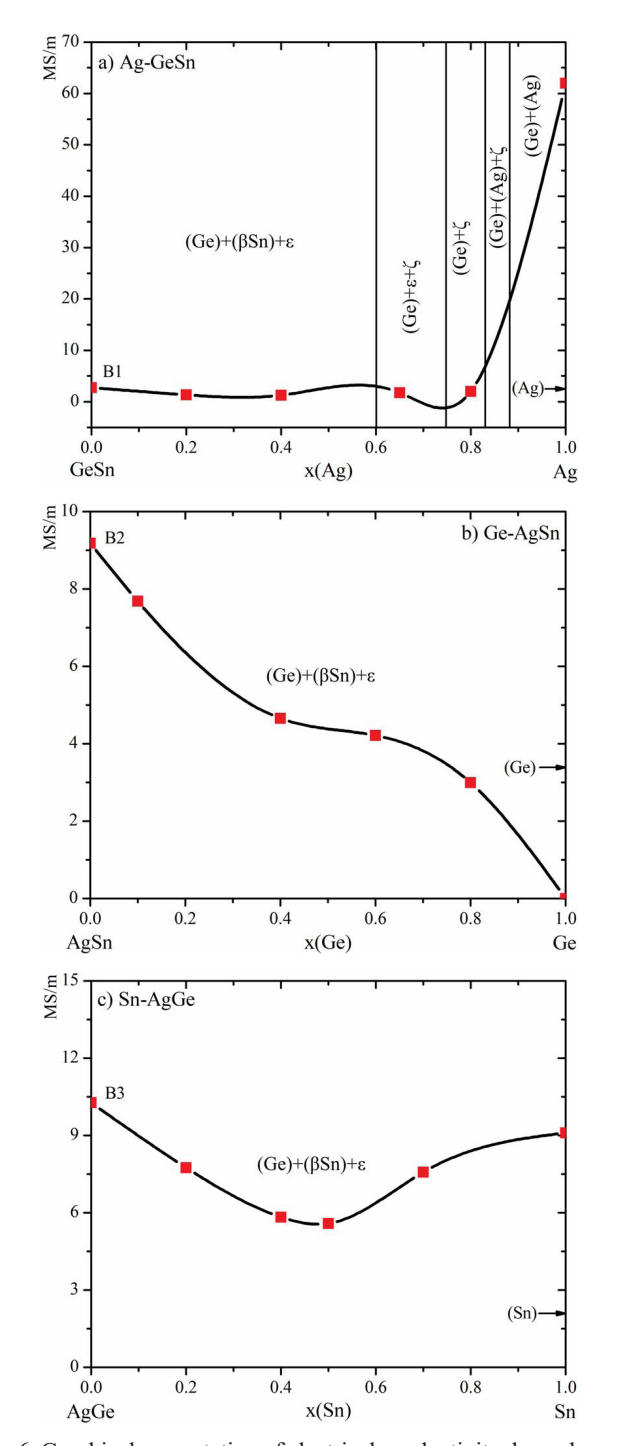


Fig. 6. Graphical presentation of electrical conductivity dependence of composition and phase fraction a) vertical section Ag-GeSn, b) vertical section Ge-AgSn and c) vertical section Sn-AgGe [11]

the electrical conductivity values showed relatively low results with small variations, so it can be concluded that the alloy composition does not play a significant role in this case.

The same approach was used to develop models for predicting electrical conductivity. The Reduced Cubic Cox Mixture model was selected as the final equation for conductivity prediction. ANOVA (Analysis of Variance) confirmed the suitability of the mathematical model. However, statistical analysis revealed that the distribution of residuals was not normal, indicating the need to transform the mathematical model to satisfy normality

conditions. The Box-Cox diagnostic recommended using the "Power" transformation to stabilize the variance.

The final equation for the predictive model in terms of real components is:

$$Ln (EP + 1.00) = 4.036388638 \cdot (Ag) - 0.137064739 \cdot (Ge)$$

$$+ 2.175797172 \cdot (Sn) + 0.463525434 \cdot (Ag) \cdot (Ge)$$

$$- 4.099509193 \cdot (Ag) \cdot (Sn)$$

$$- 16.81004221 \cdot (Ag) \cdot (Ge) \cdot (Ag-Ge)$$

$$- 11.38241626 \cdot (Ag) \cdot (Sn) \cdot (Ag-Sn)$$
(8)

The repeated analysis for Power model transformation confirms the significance of the Transformed Reduced Cubic Slack Mixture. In this case, ANOVA confirms the adequacy of Reduced Cubic Slack Mixture model (TABLE 7).

TABLE 7
ANOVA for Reduced Cubic Cox Mixture model

Source	Sum of Squares	df	Mean Square	F Value	<i>p</i> -value Prob > <i>F</i>	
Model	10.8686	6	1.81143	7.91071	0.00176	
Linear Mixture	4.8815	2	2.44076	10.65910	0.00267	
AB	0.0131	1	0.01311	0.05726	0.81528	
AC	1.0967	1	1.09675	4.78962	0.05110	
AB(A-B)	1.5592	1	1.55920	6.80922	0.02428	
AC(A-C)	0.6971	1	0.69710	3.04430	0.10886	
Residual	2.5188	11	0.22898			
Cor Total	13.3874	17				

The *F*-value of the Model is 7.91 and it implies that the model is significant. *R*-squared and other statistics after the ANOVA have good values which confirm the justification of the choice of the adopted mathematical model (TABLE 8).

TABLE 8
R-squared and other statistics after the ANOVA

Std. Dev.	0.47852	R-Squared	0.81185
Mean	1.74228	Adj R-Squared	0.70922
C.V. %	27.46533	Pred R-Squared	0.45596
PRESS	7.28325	Adeq Precision	13.98557

The diagnosis of the statistical properties of the assumed model found that the distribution of residuals are normal. After the applied Box-Cox procedure, the value of λ is 0.0, the optimum value of λ is 0.01 and the 95% confidence interval for λ (Low C.I. = -0.66, High C.I. = 0.55) contains the value 0.0, thus proving the justification of the model transformation.

Iso-lines contour plot for Electrical conductivity of Ag-Ge-Sn alloys defined by Eq. (8) is shown in Fig. 7.

3.4. Corrosion resistance

The corrosion resistance results presented here are based on our previous studies, with additional clarifica-

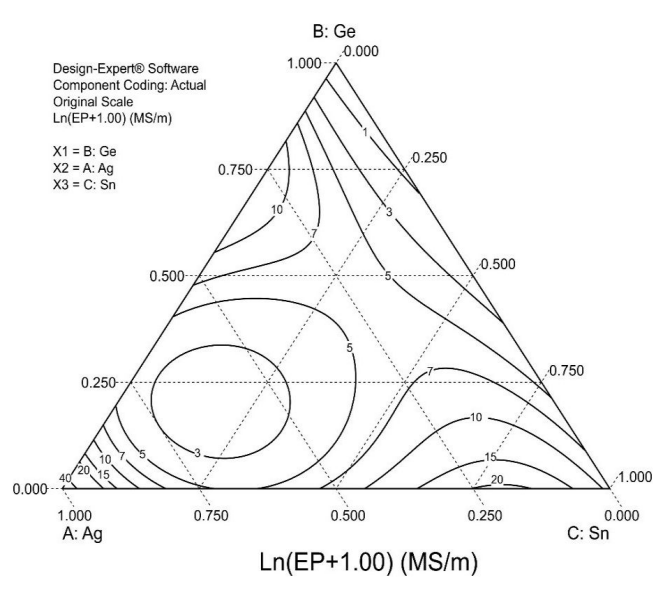


Fig. 7. Calculated iso-lines of Electrical conductivity in ternary Ag-Ge-Sn system

tions [12]. For the corrosion resistance tests, three binary alloys (Ge50Sn50, Ag50Sn50, Ag50Ge50) and six ternary alloys (sample 3: Ag65Ge17.5Sn17.5, sample 4: Ag80Ge10Sn10, sample 5: Ag45Ge10Sn45, sample 6: Ag30Ge40Sn30, sample 11: Ag25Ge25Sn50, and sample 12: Ag15Ge15Sn70) were selected. The Tafel plots are shown in Figs 8. and 9, while the corresponding Nyquist diagrams are presented in Figs. 10 and 11. TABLES 9 and 10 summarize the electrochemical polarization parameters obtained for corrosion, including the corrosion potential (E_corr), corrosion current density (E_corr), anodic E_corr 0, and cathodic E_corr 1 is also provided. Electrochemical impedance parameters for corrosion are presented in TABLES 11 and 12.

From the presented data (Fig. 8 and TABLE 9) for the tested samples of three binary alloys B1 Ge $_{50}$ Sn $_{50}$, B2 Ag $_{50}$ Sn $_{50}$ and B3 Ag $_{50}$ Ge $_{50}$ it is evident that the corrosion potentials of $E_{_corr}$ range from -296 mV for B3 Ag $_{50}$ Ge $_{50}$ to -482 mV for B2 Ag $_{50}$ Sn $_{50}$. The $j_{_corr}$ corrosion current densities range from $1.060~\mu\text{A/cm}^2$ for B3 Ag $_{50}$ Ge $_{50}$ to $16.10~\mu\text{A/cm}^2$ for B1 Ge $_{50}$ Sn $_{50}$. The lowest value of corrosion rate $v_{_corr} = 0.035~\text{mm/year}$ is for the binary alloy B3 Ag $_{50}$ Ge $_{50}$, which is more corrosion resistant than the binary alloy B1 Ge $_{50}$ Sn $_{50}$ ($v_{_corr} = 0.54~\text{mm/year}$) and the binary alloy B2 Ag $_{50}$ Sn $_{50}$ ($v_{_corr} = 0.098~\text{mm/year}$), which has the highest value of the corrosion rate of the three binary alloys tested.

Based on the presented data (Fig. 9 and TABLE 10) of the tested alloys of the ternary Ag-Ge-Sn system, the highest

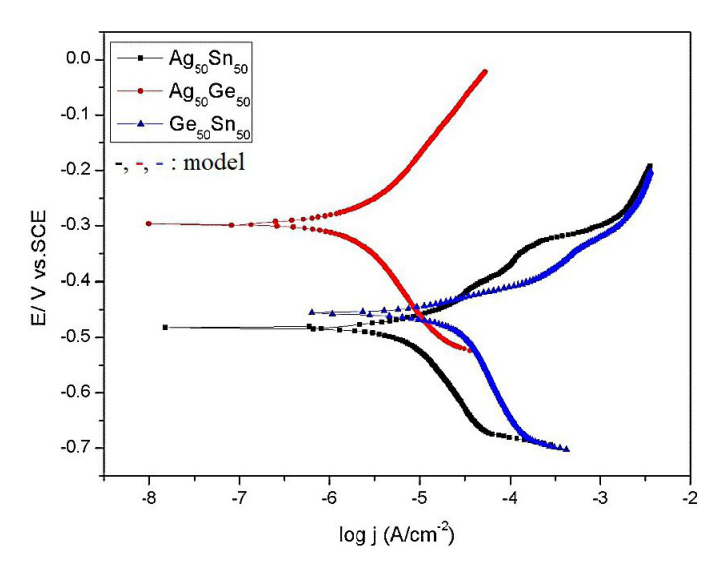


Fig. 8. Tafel plots for tested binary alloys $Ge_{50}Sn_{50}, Ag_{50}Ge_{50}, Ag_{50}Sn_{50}$ [12]

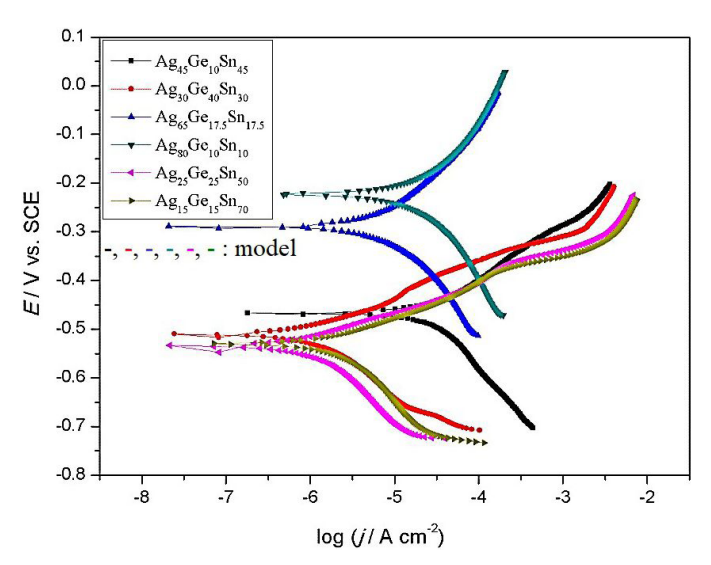


Fig. 9. Tafel plots for tested ternary alloys AgGeSn [12]

corrosion resistance was shown by sample 6 (Ag₃₀Ge₄₀Sn₃₀), with corrosion potential $E_{_corr} = -509$ mV, the lowest corrosion density $j_{_corr} = 0.16 \,\mu\text{A/cm}^2$ and the lowest corrosion rate $v_{_corr} = 0.005$ mm/year. Compared with other samples percent of (Ge) phase is highest in sample 6 and then decreases. Sample 11 (Ag₂₅Ge₂₅Sn₅₀) also show very high corrosion resistance, where the corrosion current densities are $j_{_corr} = 0.22 \,\mu\text{A/cm}^2$ and corrosion rate $v_{_corr} = 0.007$ mm/year. Based on the corrosion current density and the calculated depth indicator of corrosion-corrosion rate $v_{_corr}$ all tested alloys are very resistant to cor-

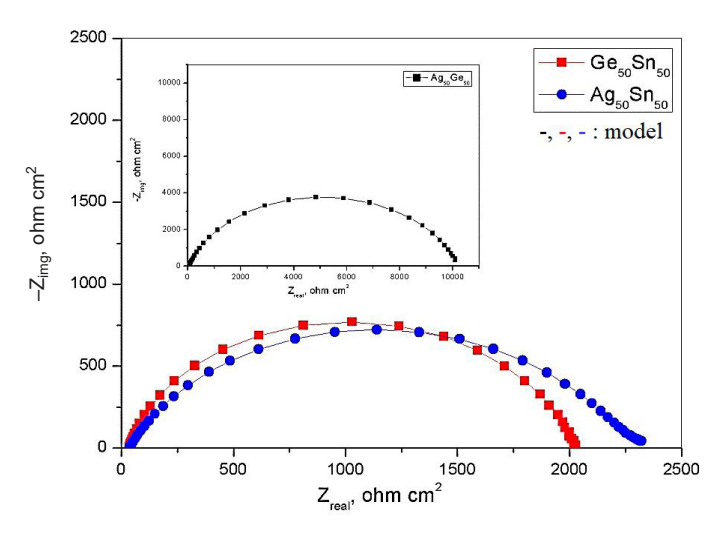
TABLE 9

Electrochemical polarization parameters of corrosion for tested binary alloys $Ge_{50}Sn_{50}$, $Ag_{50}Ge_{50}$, and $Ag_{50}Sn_{50}$ [12]

Alloy	Content of the phase at 25°C	E_corr (mV)	j_corr (μA/cm²)	v_corr (mm/year)	βa (mV/s)	βk (mV/s)
B1, Ge ₅₀ Sn ₅₀	$50\%(Ge) + 50\%(\beta Sn)$	456	16.10	0.54	73.40	105.8
B2, Ag ₅₀ Sn ₅₀	33%(βSn) + 67%ε	482	2.940	0.098	37.40	57.90
B3, Ag ₅₀ Ge ₅₀	50%(Ag) + 50%(Ge)	296	1.060	0.035	84,40	114.3

Electrochemical polarization parameters of corrosion for tested ternary alloys AgGeSn [12]

Alloy	Content of the phase at 25°C	$E_{_corr}$ (mV)	$j_{_corr} (\mu A/cm^2)$	v_corr (mm/year)	βa (mV/s)	βk (mV/s)
$3 - Ag_{65}Ge_{17,5}S_{n17,5}$	$17\%(Ge) + 53\%\epsilon + 30\%\zeta$	289	0.94	0.031	32.66	67.76
$4 - Ag_{80}Ge_{10}Sn_{10}$	$10\%(\text{Ge}) + 90\%\zeta$	224	2.67	0.089	33.66	68.61
$5 - Ag_{45}Ge_{10}Sn_{45}$	$30\%(\beta \text{Sn}) + 10\%(\text{Ge}) + 60\%\varepsilon$	466	3.859	0.129	25.33	67.22
$6 - Ag_{30}Ge_{40}Sn_{30}$	$20\%(\beta \text{Sn}) + 40\%(\text{Ge}) + 40\%\varepsilon$	509	0.16	0.005	24.39	49.77
$11 - Ag_{25}Ge_{25}Sn_{50}$	$42\%(\beta \text{Sn}) + 25\%(\text{Ge}) + 33\%\varepsilon$	533	0.22	0.007	38.58	53.59
$12 - Ag_{15}Ge_{15}Sn_{70}$	$65\%(\beta \text{Sn}) + 15\%(\text{Ge}) + 20\%\varepsilon$	529	0.42	0.013	37.12	51.33



8000 Ag₄₅Ge₁₀Sn₄₅ 7000 Ag₃₀Ge₄₀Sn₃₀ Ag₆₅Ge_{17.5}Sn_{17.5} 6000 Ag₈₀Ge₁₀Sn₁₀ - $\mathsf{Z}_{\mathsf{img}}$, ohm c m^2 Ag₂₅Ge₂₅Sn₅₀ 5000 Ag, Ge, Sn, 4000 -, -: model 3000 2000 1000 4000 5000 6000 7000 Z_{real}, ohm cm²

Fig. 10. Nyquist diagrams for tested binary alloys B1-Ge $_{50}$ Sn $_{50}$, B2-Ag $_{50}$ Sn $_{50}$ and B3-Ag $_{50}$ Ge $_{50}$ [12]

Fig. 11. Nyquist diagrams for tested ternary alloys of the Ag-Ge-Sn system [12]

rosion ($v_{corr} = 0.005$ -0.129 mm / year) in 3% NaCl solution. The corrosion resistance of the tested alloys decreases in the following order: sample $6(Ag_{30}Ge_{40}Sn_{30})$, $11(Ag_{25}Ge_{25}Sn_{50})$, $12(Ag_{15}Ge_{15}Sn_{70})$ $3(Ag_{65}Ge_{17.5}Sn_{17.5})$, $4(Ag_{80}Ge_{10}Sn_{10})$ and $5(Ag_{45}Ge_{10}Sn_{45})$. Similar trend is relating to reduction of (Ge) phase: 6, 11, 3, 12, 4 and 5. Based on the data, sample 6 demonstrates the highest corrosion resistance, attributed to its high percentage of the (Ge) phase, with the lowest corrosion potential, current density, and corrosion rate. In contrast, all tested alloys

show strong corrosion resistance, with corrosion rates ranging, with sample 6 exhibiting the best overall performance.

Nyquist diagrams for three samples of binary alloys and six samples of ternary alloys were recorded by electrochemical impedance spectroscopy (EIS) (Figs. 10 and 11). The fitting of the experimental data was done using an equivalent circuit (Fig. 12) and the results (electrochemical impedance corrosion parameters) are shown in TABLES 11 and 12.

TABLE 11 Electrochemical impedance corrosion parameters for tested binary alloys B1-Ge₅₀Sn₅₀, B2-Ag₅₀Sn₅₀ and B3-Ag₅₀Ge₅₀ [12]

Alloy	$R_{soln}, (\Omega)$	R_{cor} , (Ω)	$R_{po},(\Omega)$	$R_{tot.}(\Omega)$	C_{cor} , (F)	n	C_c , (F)	m	Fitting error
B1-Ge ₅₀ S _{n5} 0	65.15	635,3	1672	2307.3	$9.70 \cdot 10^{-4}$	0.846	$2.10 \cdot 10^{-5}$	0.773	2.985 · 10 ⁻⁴
B2-Ag ₅₀ Sn ₅₀	35.41	3233	1870	5103.0	$1.52 \cdot 10^{-2}$	0.525	$6.34 \cdot 10^{-6}$	0.743	$1.598 \cdot 10^{-4}$
B3-Ag ₅₀ Ge ₅₀	34.94	10050	142.4	10 192.4	$1.16 \cdot 10^{-5}$	0.745	$6.06 \cdot 10^{-6}$	0.901	$1.090 \cdot 10^{-3}$

TABLE 12 Electrochemical impedance corrosion parameters for tested ternary alloys of the Ag-Ge-Sn sytem [12]

Alloy	$R_{soln}, (\Omega)$	R_{cor} , (Ω)	$R_{po},(\Omega)$	R_{tot} , (Ω)	C_{cor} , (F)	n	C_c , (F)	m	Fitting error
$3 - Ag_{65}Ge_{17,5}Sn_{17,5}$	25.42	3263	770.5	4033.5	$2.93 \cdot 10^{-4}$	0.6159	$2.39 \cdot 10^{-5}$	0.7286	$366.8 \cdot 10^{-6}$
$4 - Ag_{80}Ge_{10}Sn_{10}$	24.29	1672	25.56	1697.56	$2.51 \cdot 10^{-5}$	0.3477	$2.94 \cdot 10^{-5}$	0.8922	$150.2 \cdot 10^{-6}$
$5 - Ag_{45}Ge_{10}Sn_{45}$	32.45	642.7	171.4	814.1	$1.41 \cdot 10^{-5}$	0.4133	$4.55 \cdot 10^{-6}$	0.9635	$1.521 \cdot 10^{-3}$
$6 - Ag_{30}Ge_{40}Sn_{30}$	27.53	6567	943	7510	$3.79 \cdot 10^{-6}$	0.8792	$1.13 \cdot 10^{-5}$	0.8765	$2.541 \cdot 10^{-3}$
$11 - Ag_{25}Ge_{25}Sn_{50}$	26.88	398.3	4457	4855.3	$1.22 \cdot 10^{-4}$	0.9899	$1.30 \cdot 10^{-6}$	0.8835	$3.269 \cdot 10^{-4}$
$12 - Ag_{15}Ge_{15}Sn_{70}$	26.32	3234	1605	4839	$1.54 \cdot 10^{-6}$	0.9613	$2.38 \cdot 10^{-5}$	0.8531	$4.245 \cdot 10^{-3}$

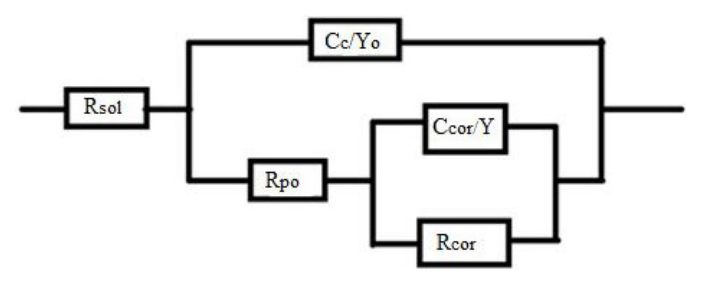


Fig. 12. Equivalent circuit [12]

The experimental data were fitted using the Gamry Echem Analyst software and the equivalent circuit shown in Fig. 12. In this model, R_{sol} represents the resistance of the electrolyte, R_{po} denotes the pore resistance (the film formed on the electrode surface), and R_{cor} refers to the resistance to charge transfer. C_{cor} and C_c are the electrochemical capacitance and film capacitance, respectively [38]. The exponents n and m are frequently used to identify the mechanism that controls the electrochemical reaction rate in a particular system.

The value of n ranges from 0 to 1, reflecting the inherent physical and chemical heterogeneity of the solid surface, as well as the presence of a porous product layer or a current density distribution across the surface [39]. When n values range from 0.70 to 0.90, it indicates that the corrosion rate is primarily determined by slow charge transfer. On the other hand, a value below 0.7 suggests that the electrochemical process is governed by diffusion control [40].

Due to the scattering effect caused by surface imperfections, the constant phase element of the CPU is used as a replacement for the capacitor to fit the EIS data more accurately [41].

The impedance of the phase element (Z_{CPE}) is expressed as follows [42,43].

$$Z_{CPE} = \frac{1}{Y_0} (j\omega)^n \tag{9}$$

where:

 Y_0 – proportionality factor – magnitude of the CPU,

j – imaginary unit,

 ω - angular velocity,

n – phase shift (CPE exponent).

A phase element (CPE) was used to fit the data, which can be treated as a parallel combination of a pure capacitor and a resistor that is inversely proportional to the angular frequency, and when the factors n and m are equal to one, CPE acts as a capacitor, whereas if n, m = 0, then CPE acts as a resistor.

The constant phase element consists of the constant *Y* and the exponent *n*, which quantifies various physical phenomena, such as inhomogeneity of the electrode surface due to surface roughness, adsorption of inhibitors, formation of porous layers, etc. [44].

When fitted with a phase element (CPE), Y_0 is obtained, not the capacitance value. If n, m = 0.8-1, then the capacitance does

not have to be recalculated, but the obtained value Y_0 is taken as the value of capacitance. If n, m < 0.8, then the recalculation is performed.

As a known electrical parameter, the value of the capacitance C_i according to equation [45] can be calculated:

$$C_i = \left(Y_{0i} R_i^{1 - n_i}\right)^{1/n_i} \tag{10}$$

and C_c and C_{cor} were calculated from it:

$$C_c = \left(Y_1 R_{po}^{1-m}\right)^{1/m} \tag{11}$$

$$C_{cor} = \left(Y_2 R_{cor}^{1-n}\right)^{1/n} \tag{12}$$

where: R_i – resistors, and Y_0 and n are modules.

The total resistance (R_{tot}) is calculated by the following equation [46].

$$R_{tot} = R_{po} + R_{cor} \tag{13}$$

sample (working electrode) and approximately the same values will hold for all the samples resistance does not depend on the corrosion process on the metal.

From the recorded Nyquist diagrams (Fig. 11) and fitting the experimental results, for binary alloys, the calculated values of R_{tot} shown in TABLE 11 decrease in the following order: $Ag_{50}Ge_{50} > Ag_{50}Sn_{50} > Ge_{50}Sn_{50}$. This is in accordance with the calculated corrosion rate v_{corr} (mm/year) for these binary alloys obtained from Tafel plots (TABLE 9). The values of exponent n shown in TABLE 11 confirm that the corrosion rate for the $Ag_{50}Sn_{50}$ binary alloy is under diffusion control while the values for the $Ag_{50}Ge_{50}$ and $Ge_{50}Sn_{50}$ binary alloys indicate that the corrosion rate is determined by the slow charge transfer rate.

Based on the recorded Nyquist diagrams of Fig. 11 and the fitting of the experimental results for the six tested ternary Ag-Ge-Sn alloys, the calculated values of total resistance R_{tot} shown in TABLE 12 decrease in the following order: alloy $Ag_{30}Ge_{40}Sn_{30}$, $Ag_{25}Ge_{25}Sn_{50}$, $Ag_{15}Ge_{15}Sn_{70}$, $Ag_{65}Ge_{17.5}Sn_{17.5}$, Ag₈₀Ge₁₀Sn₁₀, Ag₄₅Ge₁₀Sn₄₅, which is in accordance with the calculated corrosion rate $v_{_corr}$ (mm/year) obtained from Tafel plots (TABLE 10). The values of exponent n shown in TABLE 12 confirm that the corrosion rate for alloys $Ag_{45}Ge_{10}Sn_{45},\,Ag_{65}Ge_{17.5}Sn_{17.5}$ and $Ag_{80}Ge_{10}Sn_{105}Sn_{30}$ is under diffusion control while the values for alloys Ag₃₀Ge₄₀Sn₃₀, Ag₂₅Ge₂₅Sn₅₀, and Ag₁₅Ge₁₅Sn₇₀ indicate that the corrosion rate is determined by the slow charge transfer rate. High values of R_{po} are associated with the porosity of the passive film. Given the relative resistance ratios R_{po} and R_{cor} , it can be said that none of the tested alloys will corrode uniformly.

For the analyzed data using the equivalent circuit of Fig. 12, a low value of the error estimation of the fitting procedure was obtained (TABLES 11 and 12). It can be concluded that the selected equivalent circuit is sufficiently precise to describe the tested alloys.

3.5. Isothermal section at 500°C

Five ternary samples were annealed at 500°C for six weeks and then analyzed by using SEM-EDS and XRD techniques. The annealing of alloys at 500°C for six weeks was chosen based on previous experiences with ternary alloys. Annealing at 500°C facilitated the formation of various coexisting phases, which were of interest for detailed investigation in this study. The extended annealing period of six weeks allows for the stabilization of microstructures and the formation of solid phases, providing more precise and reliable results when analyzed using SEM-EDS and XRD techniques. Experimental results are summarized in TABLE 13.

The overall compositions of the annealed samples were determined by mapping the entire polished surfaces of the samples. By contrast, the compositions of the observed coexisting phases were determined examining the surface of the same phase at different parts of the sample (at least five different positions of the same phase were examined per phase). The chemical compositions of the phases determined in this study represented the mean values based on at least five individual analyses.

The recorded XRD patterns were subsequently analyzed using TOPAS 4.2 software and the International Centre for Diffraction Data (ICDD) Powder Diffraction Files (PDF2) database (2020). The lattice parameters were determined using TOPAS software and by performing full Rietveld refinement.

With five analyzed samples, three different phase regions were detected. Samples 1, 2 and 3 have liquid phase L and (Ge) solid solution in the microstructure. Liquid phase is rich with tin, about 9 at.% silver and small amounts of germanium \approx 2at.%, while (Ge) solid solution phase is rich with germanium and with neglected solubility of silver and tin. Detected phases in the microstructure of the sample 4 are liquid phase, (Ge) and ζ . Liquid phase is rich with tin 85.40 at.%, some amount of silver 10.15 at.% and left over is germanium 4.45 at.%. Phase (Ge) solid solution is rich with germanium 98.76 at.% and left over

are neglected amount of silver and tin. Phase ζ is rich with silver (81.77 at.%) and tin (18.12 at.%) and neglected amount of germanium (0.11 at.%). Sample 5 have two phases in microstructure (Ag) and (Ge) solid solutions. Solubility of silver and tin in the (Ge) solid solution is negligible and solubility of tin in (Ag) solid solution is 5.19 at.% while solubility of germanium is 2.93 at.%. Three microstructures recorded by SEM are given in Fig. 13.

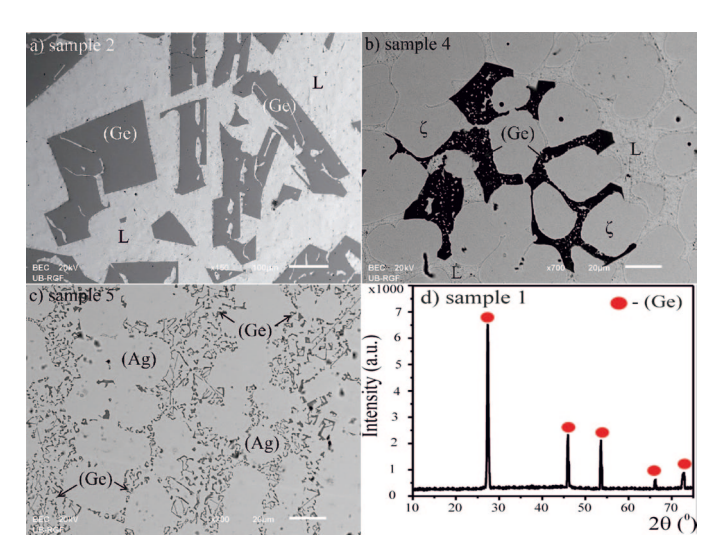


Fig. 13. SEM micrographs of the samples annealed at 500°C of a) sample 2, b) sample 4 c) sample 5 and d) XRD powder pattern of sample 1

Microstructure of sample 2 includes liquid phase L and (Ge) solid solution. (Ge) solid solution appears as a dark phase, liquid phase as a light phase. Sample 4 includes liquid phase as a light phase, (Ge) solid solution as a dark phase and ζ intermetallic compound as a gray phase in the microstructure. In the microstructure of sample 5, (Ge) phase appears as a dark phase while (Ag) phase is a light phase.

EDS results, given in TABLE 13, are compared with calculated isothermal section at 500°C (Figure 14).

TABLE 13 Combined results of SEM-EDS and XRD analyzes of the selected Ag-Ge-Sn alloys annealed at $T=500^{\circ}$ C

N.	Composition of samples	Determined phases		Compositions of phases (at.%)			Lattice parameters (Å)	
	(at. %)	EDS	XRD	Ag	Ge	Sn	а	С
	9.21 Ag	L		9.44±0.4	2.08±0.2	88.48±0.3		
1.	70.63 Ge	(Ge)	(Ge)	0.30 ± 0.1	99.21±0.2	0.49±0.3	5.6522 ± 0.0002	
	20.16 Sn			3.26±0.7	1.62±0.6	95.12±0.4		
	14.11 Ag	L		7.88±0.1	2.10±0.6	90.02±0.4		
2.	26.26 Ge	(Ge)	(Ge)	1.62±0.7	98.16±0.8	0.22±0.5	5.6536 ± 0.0008	
	59.63 Sn			2.91±0.3	0.96 ± 0.8	96.13±0.6		
	34.62 Ag	L		7.14±0.8	2.88±0.9	89.98±0.7		
3.	22.43 Ge	(Ge)	(Ge)	0.61±0.6	98.18±0.5	1.21±0.8	5.6512 ± 0.0009	
	42.95 Sn							
	50.24 Ag	L		10.15±0.5	4.45±0.2	85.40±0.9		
4.	25.87 Ge	(Ge)	(Ge)	0.82±0.5	98.76±0.4	0.42±0.8	5.6597 ± 0.0004	
	23.89 Sn	ζ	ζ	81.77±0.9	0.11±0.6	18.12±0.3	2.9632 ± 0.0005	4.7876 ± 0.0003
	68.02 Ag	(Ag)	(Ag)	91.88±0.3	2.93±0.7	5.19±0.4	4.0743 ± 0.0008	
5.	26.34 Ge	(Ge)	(Ge)	0.79±0.6	99.02±0.2	0.19±0.6	5.6533 ± 0.0006	
	5.64 Sn							

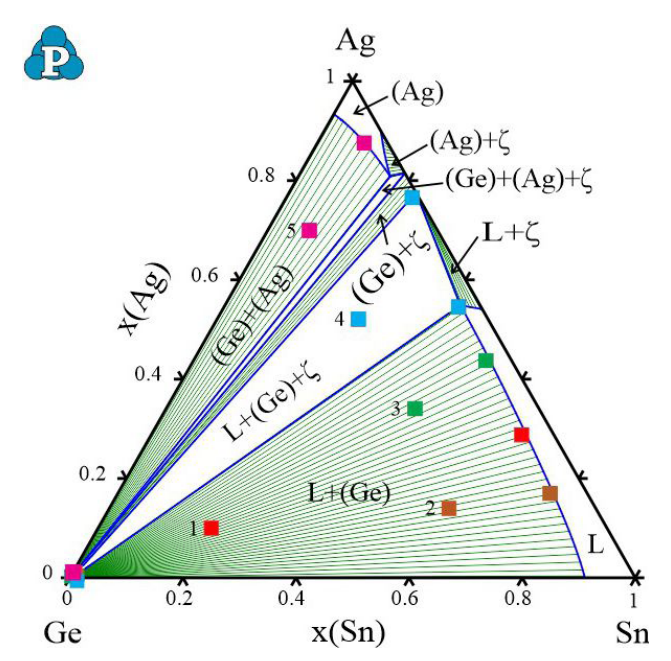


Fig. 14. Calculated isothermal section at 500°C compared with EDS results given in TABLE 13

Nine different phase regions are calculated for isothermal section at 500°C. Two are single-phase regions (L and (Ag)), five are two-phase regions (L + (Ge), $L + \zeta$, (Ge) + ζ , (Ag) + ζ and (Ge) + (Ag)) and two are three-phase regions ($L + (Ge) + \zeta$ and (Ge) + (Ag) + ζ). Three of these nine phase regions are experimentally confirmed. By comparing experimental results and calculation a good agreement has been reached.

4. Conclusion

The ternary Ag-Ge-Sn system has been experimentally investigated by using several experimental techniques: SEM-EDS, XRD, corrosion test, hardness measurements by Brinell method and electrical conductivity measurements.

The isothermal section at 500°C, is experimentally investigated by XRD and SEM-EDS techniques. Experimental results were compared with calculated phase diagram at 500°C and good agreement between data is reached. Nine different phase regions are calculated for isothermal section at 500°C. Two are single-phase regions, five are two-phase regions and two are three-phase regions. Three of these nine phase regions are experimentally confirmed. By comparing experimental results and calculation a good agreement has been reached.

Experimentally determined phases by XRD analysis were compared with calculated isothermal section at 25°C and agreement between the results was reached. The calculated isothermal section at 25°C presents five different phase regions. Two are two-phase regions, while three are three-phase regions. Based on the composition of the samples, the existence of three regions was confirmed: two two-phase regions and one three-phase region. Experimentally determined compositions of coexisting phases were in good agreement with related calculated compositions.

Conducted experiments did not indicate any new ternary phases or large solubility of third element in binary phases.

Microstructural, hardness, electrical conductivity tests were performed on twelve ternary alloys. Results of Brinell hardness and electrical conductivity measurements were presented and discussed with respect to alloys compositions and phase constituents. Overall, it can be concluded that the percentage of the (Ge) phase significantly influences the hardness values. The hardness of the samples is strongly influenced by their phase composition. A higher proportion of the (Ge) phase leads to increased hardness. The electrical conductivity values showed relatively low results with small variations from 1.264 to 7.741 MN/m².

By using appropriated mathematical model these properties were predicted in the whole composition range. The corrosion resistance of six ternary and three binary alloys was examined in 3% NaCl solution using the potentiodynamically polarization method (Tafel plots) and electrochemical impedance spectroscopy (EIS). The highest corrosion resistance is for sample 6 (Ag30Ge40Sn30). In contrast, all tested alloys show strong corrosion resistance, with corrosion rates ranging, with sample 6 exhibiting the best overall performance.

In general, it can be concluded that high hardness alloys lead to low electrical conductivity. This trend is visible for alloys 5 to 8. Alloy 5 has low hardness while electrical conductivity is high. While alloy 8 have high hardness and low electrical conductivity. According to the corrosion resistance $E_{_corr}$ is higher for alloy with lower hardness.

Acknowledgments

This work has been supported by the National Nature Science Foundation of China (project No.51950410600) and the Ministry of Education, Science and Technological Development of the Republic of Serbia (Grant No. OI172037). The research presented in this paper was done with the financial support of the Ministry of Education, Science and Technological Development of the Republic of Serbia, within the funding of the scientific research work at the University of Belgrade, Technical Faculty in Bor, according to the contract with registration number 451-03-68/2020-14/200131.

REFERENCE

- [1] V. Ponnambalam, D.T. Morelli, A novel method to synthesize bulk super saturated solid solutions Ge1–xSnx ($x \le 5.0\%$). J. Alloys Compd. 740, 42-46 (2018).
 - DOI: https://doi.org/10.1016/j.jallcom.2017.12.351
- [2] R. Goswami, S.B. Qadri, E.P. Gorzkowski, J.P. Yesinowski, G.G. Jernigan, Stabilization of Diamond Cubic Sn Nanodots in Ge. Mater Lett. 187, 126-128 (2017).
 - DOI: https://doi.org/10.1016/j.matlet.2016.10.061\
- P. Moontragoon, N. Vukmirovic, Z. Ikonic, P. Harrison, Electronic structure and optical properties of Sn and SnGe quantum dots.
 J. Appl. Phys. 103, 1037121-1037128 (2008).
 DOI: https://doi.org/10.1063/1.2932169

- [4] D. Ielmini, A.L. Lacaita, Phase change materials in non-volatile storage. Mater. Today. 14, 600-607 (2011).
 DOI: https://doi.org/10.1016/S1369-7021(11)70301-7
- J.M. del Pozo, L.Díaz, Optical study of Ge(1x)Sb(x) crystalli- zation. J. Non-Cryst. Solids. 243, 5-51 (1999).
 DOI: https://doi.org/10.1016/S0022-3093(98)00816-3
- [6] E.M. Vinod, R. Naik, R. Ganesan, K.S. Sangunni, Signatures of Ge2Sb2Te5 film at structural transitions. J. Non-Cryst. Solids. 358, 2927-2930 (2012). DOI: https://doi.org/10.1016/j.jnoncrysol.2012.07.021
- [7] P. Nemec, V. Nazabal, A. Moreac, J. Gutwirth, L. Benes, M. Frumar, Amorphous and crystallized Ge-Sb-Te thin films deposited by pulsed laser: Local structure using Raman scattering spectroscopy. Mater. Chem. Phys. 136, 935-941 (2012).
 DOI: https://doi.org/10.1016/j.matchemphys.2012.08.024
- [8] S. Raoux, W. Welnic, D. Lelmini, Phase Change Materials and Their Application to Nonvolatile Memories. Chem. Rev. 110, 240-267 (2010).
- [9] S.L. Ou, C.P. Cheng, C.Y. Yeh, C.J. Chung, K.S. Kao, R.C. Lin, Characteristics of In-Ge-Sb-Sn-Te Thin Film Used for Phase Change Optical Recording Media. Adv. Mater. Res. 4430-4433 (2011). DOI: https://doi.org/10.4028/www.scientific.net/AMR.189-193.4430
- [10] N. Toskovic, M. Premovic, M. Tomic, D. Minic, D. Manasijevic, M. Gorgievski, Experimental examination and thermodynamic description of the ternary Ag-Ge-Sn system. J. Chem. Thermodynamics. 131, 563-571 (2019). DOI: https://doi.org/10.1016/j.jct.2018.12.003
- [11] A. Đorđević, D. Minić, M. Zečević, D. Manasijević, Mechanical and electrical properties of the ternary Ag-Ge-Sn alloys, 54th International October Conference on Mining and Metallurgy – IOC 2023, 104-107 (2023).
- [12] M. Zečević, D. Minić, A. Đorđević, D. Manasijević, Effect of chemical composition on the corrosion resistance of the ternary Ag-Ge-Sn alloys, 54th International October Conference on Mining and Metallurgy – IOC 2023, 108-111 (2023).
- [13] W. Cao, S.L. Chen, F. Zhang, K.Wu, Y. Yang, Y.A. Chang, R. Schmid-Fetzer, W.A. Oates, PANDAT software with PanEngine, PanOptimizer and PanPrecipitation for multi-component phase diagram calculation and materials property simulation. Calphad. 33 (2), 328-342 (2009). DOI: https://doi.org/10.1016/j.calphad.2008.08.004
- [14] A. Marković, D. Minić, M. Premović, D. Manasijević, D. Guresić, M. Kolarevic, Effect of chemical composition on the microstructure, hardness and electrical conductivity profiles of the Ag-Bi-Ge Alloys. Mat. Rsrch. 22 (6), e20190372 (2019).
 DOI: https://doi.org/10.1590/1980-5373-MR-2019-0372
- [15] M. Premovic, D. Minic, Y. Du, M. Kolarevic, M. Milosavljevic, Thermodynamic description, hardness and electrical conductivity of the Bi-Ni-Zn system: Experiment and modeling. J. Alloys Compd. 825, 154156 (2020). DOI: https://doi.org/10.1016/j.jallcom.2020.154156
- [16] M. Pavlović, D. Stanojević, S. Mladenović, Korozija i zaštita materijala, Tehnološki fakultet, 2012 Zvornik.

- [17] E.E. Stansbury, R.A. Buchanan, Fundamentals of Electrochemical Corrosion, ASM International, 2000 Materials Park, Ohio.
- [18] D. Pletcher, R. Greef, R. Peat, L.M. Peter, J. Robinson, Instrumental Methods in Electrochemistry, Ellis Horwood Limited, Chichester, 2001 West Sussex.
- [19] Y. Tan, Heterogeneous Electrode Processes and Localized Corrosion, 2013 John Wiley & Sons, Inc., Hoboken, New Jersey.
- [20] D. Landolt, Corrosion and Surface Chemistry of Metals, 2007 EPFL Press.
- [21] A. Lasia, Electrochemical Impedance Spectroscopy and its Applications, 2014 Springer, New York.
- [22] M.E. Straumanis, Neubestimmung der Gitterparameter, Dichten und thermischen aus dehnungs koeffizienten von silber und gold, und vollkommenheit der struktur. Monatsh. Chem. 102, 1377-1386 (1971). DOI: https://doi.org/10.1007/BF00917194
- [23] V.T. Deshpande, D.B. Sirdeshmukh, Thermal expansion of tetragonal tin. Acta Crystallogr. 14, 355-356 (1961).DOI: https://doi.org/10.1107/S0365110X61001212
- [24] J. Thewlis, A.R. Davy, Thermal expansion of grey tin. Nature. 174, 1011 (1954). DOI: https://doi.org/10.1038/1741011a0
- [25] A.S. Cooper, Precise lattice constants of germanium, aluminum, gallium arsenide, uranium, sulphur, quartz and sapphire. Acta Crystallogr. 15, 578-582 (1962).
 DOI: https://doi.org/10.1107/S0365110X62001474
- [26] H.W. King, T.B. Massalski, Lattice spacing relationships and the electronic structure of h.c.p. zeta-phases based on silver. Philos. Mag. 8, 669-682 (1961). DOI: https://doi.org/10.1080/14786436108244417
- [27] C.W. Fairhurst, J.B. Cohen, The crystal structure of two compounds found in dental amalgam: Ag2 Hg3 and Ag3 Sn. Acta Crystallogr. B 28, 371-378 (1972).
 DOI: https://doi.org/10.1107/S0567740872002432
- [28] A. Đorđević, M. Premović, D. Minić, M. Tomović, B. Radičević, N. Kolarević, Mechanical and electrical properties of the Bi-Ge-Sn alloys. Met. and Mat. Eng. 26 (4), 395-412 (2020). DOI: https://scidar.kg.ac.rs/handle/123456789/20386
- [29] http://www.webelements.com/periodicity/hardness brinell/
- [30] A. Marković, M. Premović, D Minić, D. Guresic, D. Manasijević, A. Djordjević, Effect of Chemical Composition on the Microstructure and Properties of the Ag-Ga-Ge Alloys. J. of Materi Eng and Perform. 28, 3759-3766 (2019). DOI: https://doi.org/10.1007/s11665-019-04118-8
- [31] M. J. Anderson, P. J. Whitcomb, RSM Simplified, Optimizing Processes Using Response Surface Methods for Design of Experiments, 2017 CRC Press, Taylot & Francis Group.
- [32] G.E.P. Box, N.R. Draper, Response Surfaces, Mixtures, and Ridge Analyses, 2007 Wiley.
- [33] Stat-Ease, Handbook for Experimenters, Version 11.00, 2018 Stat-Ease, Inc.
- [34] D.C. Montgomery, Design and Analysis of Experiments, 2017 Wiley.
- [35] R.H. Myers, D.C. Mongomery, C.M. Anderson-Cook, Response Surface Methodology, Process and Product Optimization Using Designed Experiments, 2016 Wiley.

- [36] J. Stanić, Metod inženjerskih merenja, Mašinski fakultet, V Prerađeno i dopunjeno izdanje, 1990 Beograd.
- [37] http://periodictable.com/Properties/A/ElectricalConductivity.
- [38] S. Mallick, Z. Ahmad, F. Touati, J. Bhadra, R.A. Shakoor, N.J. Al-Thani, PLA-TiO2 nanocomposites: Thermal, morphological, structural, and humidity sensing properties Ceram. Int. 44, 16507-16513 (2018). DOI: https://doi.org/10.1016/j.ceramint.2018.06.068
- [39] D.Q. Zhang, L.X. Gao, G.D. Zhou, Inhibition of Copper Corrosion in Aerated Hydrochloric Acid Solution by Heterocyclic Compounds Containing a Mercapto Group. Corros. Sci. 46, 3031-3040 (2004).
 - DOI: https://doi.org/10.1016/j.corsci.2004.04.012
- [40] C.C. Li, X.Y. Guo, S. Shen, P. Song, T. Xu, Y. Wen, H.F. Yang, Adsorption and corrosion inhibition of phytic acid calcium on the copper surface in 3 wt% NaCl solution. Corros. Sci. 83, 147-154 (2014). DOI: https://doi.org/10.1016/j.corsci.2014.02.001
- [41] A. Popova, S. Raicheva, E. Sokolova, M. Christov, Frequency Dispersion of the Interfacial Impedance at Mild Steel Corrosion in Acid Media in the Presence of Benzimidazole Derivatives. Langmuir. 12, 2083-2089 (1996).
 - DOI: https://doi.org/10.1021/la950148 +

- [42] A. Popova, E. Sokolova, S. Raicheva, M. Christov, AC and DC Study of the Temperature Effect on Mild Steel Corrosion in Acid Media in the Presence of Benzimidazole Derivatives. Corros. Sci. 45, 33-58 (2003).
 - DOI: https://doi.org/10.1016/S0010-938X(02)00072-0
- [43] H.Y. Ma, S.H. Chen, B.S. Yin, S.Y. Zhaom, X.Q. Liu. Corros. Sci.
 45, 867-882 (2003).
 DOI: https://doi.org/10.1016/S0010-938X(02)00175-0
- [44] S. Deng, X. Li, X. Xie, Hydroxymethyl urea and 1,3-bis(hydroxymethyl) urea as corrosion inhibitors for steel in HCl solution. Corros. Sci. 80, 276-289 (2014).
 - DOI: https://doi.org/10.1016/j.corsci.2013.11.041
- [45] C.W. Yan, H.C. Lin, C.N. Cao, Investigation of inhibition of 2-mercaptobenzoxazole for copper corrosion. Electrochim. Acta. 45, 2815-2821 (2000).
 - DOI: https://doi.org/10.1016/S0013-4686(00)00385-6
- [46] R. Zhang, Z. Zhu, X. Leng, J. Pan, Y. Zhang, Corrosion characteristic of Cu-10Ni-Fex in 3.5 % NaCl. Int. J. Electrochem. Sci. 13, 11526-11538 (2018).
 - DOI: https://doi.org/10.20964/2018.12.11